ARTICLE

Check for updates

A hybrid quantum-classical method for electron-phonon systems

M. Michael Denner [1], Alexander Miessen [2,3], Haoran Yan[4,5], Ivano Tavernelli [2], Titus Neupert[1], Eugene Demler[6] & Yao Wang [4,5 ✉]

Interactions between electrons and phonons play a crucial role in quantum materials. Yet, there is no universal method that would simultaneously accurately account for strong electron-phonon interactions and electronic correlations. By combining methods of the variational quantum eigensolver and the variational non-Gaussian solver, we develop a hybrid quantum-classical algorithm suitable for this type of correlated systems. This hybrid method tackles systems with arbitrarily strong electron-phonon coupling without increasing the number of required qubits and quantum gates, as compared to purely electronic models. We benchmark our method by applying it to the paradigmatic Hubbard-Holstein model at half filling, and show that it correctly captures the competition between charge density wave and antiferromagnetic phases, quantitatively consistent with exact diagonalization.

[1] Department of Physics, University of Zurich, Winterthurerstrasse 190, 8057 Zurich, Switzerland. [2] IBM Quantum, IBM Research – Zurich, 8803 Rüschlikon, Switzerland. [3] Institute for Computational Science, University of Zurich, Winterthurerstrasse 190, 8057 Zurich, Switzerland. [4] Department of Physics and Astronomy, Clemson University, Clemson, SC 29634, USA. [5] Department of Chemistry, Emory University, Atlanta, GA 30322, USA. [6] Institute for Theoretical Physics, ETH Zürich, 8093 Zürich, Switzerland. ✉email: yao.wang@emory.edu

Understanding strongly correlated many-body systems is vital to many areas of science and technology, such as the development and analysis of functional quantum materials[1]. Due to the entanglement induced by correlations, macroscopic properties of quantum materials are often unpredictable from reductive single-particle models. Theoretical analysis of these systems with strongly entangled degrees of freedom has, however, been hindered by the exponential growth of their Hilbert space sizes with the number of particles. Understanding macroscopic properties of materials requires the analysis of sufficiently large model systems, which cannot be done accurately with classical computers. Quantum computing technologies, including hybrid quantum-classical algorithms[2–4] constitute an intriguing new direction for studying quantum many-body systems and especially quantum materials.

One of the promising representatives of hybrid algorithms is the variational quantum eigensolver (VQE)[2,5–8]. This approach aims to accurately approximate ground states of quantum systems that can be naturally represented using qubits, such as spin and fermionic models. An example of such a protocol is shown in the upper panel of Fig. 1a: one uses a set of parameterized quantum gates to prepare a variational wavefunction and measures the expectation value of the Hamiltonian; then, one optimizes the parameters of these quantum gates using a classical computer. VQE has been implemented experimentally for small molecules[9–13], providing accurate solutions verifiable by exact methods. Hardware-efficient implementations of VQE have also been proposed for solid-state systems, including quantum magnets and Mott insulators[14–17]. Successful applications of the VQE approach to describe multi-orbital molecules and intermediate-size solid-state models pave the way for extending this technique to broader classes of materials.

However, realistic materials usually contain more complex interactions than simplified electronic models, such as the Hubbard model which only features local Coulomb interaction. The interaction between mobile electrons and the ionic lattice in solids, so-called electron-phonon coupling (EPC), underlies electric and mechanical properties of materials. Notably, it has been suggested that the interplay between the electron-phonon interaction and the electronic Coulomb repulsion is crucial for many novel quantum phases, such as unconventional superconductivity in cuprates[18–23] and twisted bilayer graphene[24–29]. Achieving predictive control of these quantum phases calls for developing reliable theoretical models describing materials with EPC[30–32], which has motivated studies based on small clusters[33–35] or perturbative couplings[36–39]. Quantum simulation of materials with strong EPCs, however, remains challenging due to the unbounded phonon Hilbert space[40–43]. The common spirit of quantum algorithms is to traverse quantum states encoded by the combination of available qubits. Therefore, even with a single electronic band and single phonon mode, the system has much higher computational complexity compared to electrons alone: inclusion of phonons in an L-site spinful system increases the Hilbert-space size from 4^L (for electrons) to $4^L(m+1)^L$ where m is the (truncated) maximal local phonon occupation. For materials with non-negligible EPCs, the required $m \gg 1$ leads to an unreasonably large, and even unbounded Hilbert space. This issue prohibits not only classical simulations, but also an efficient encoding on a quantum machine.

To this end, we design a hybrid quantum algorithm which leverages the capability of VQE with quantum computers and the variational non-Gaussian description of non-perturbative polaronic dressing[44–46]. We prove the validity of our approach using the one-dimensional Hubbard-Holstein model and its variants, which is summarized together with the specifics of the algorithm in the "Methods" section. We then show that our hybrid quantum algorithm is able to reliably capture the ground-state properties of the paradigmatic Hubbard-Holstein model in all regions of the phase diagram, when compared to non-Gaussian exact diagonalization (NGSED) results. Our algorithm does not require any additional qubit overhead stemming from unbounded phononic degrees of freedom and the truncation to a low phonon occupation[40,42,43], as we implicitly sample the phonon Hilbert space. This makes it possible to analyze electron-phonon systems over a broad range of parameters, including both adiabatic and anti-adiabatic regimes of the phonon frequencies.
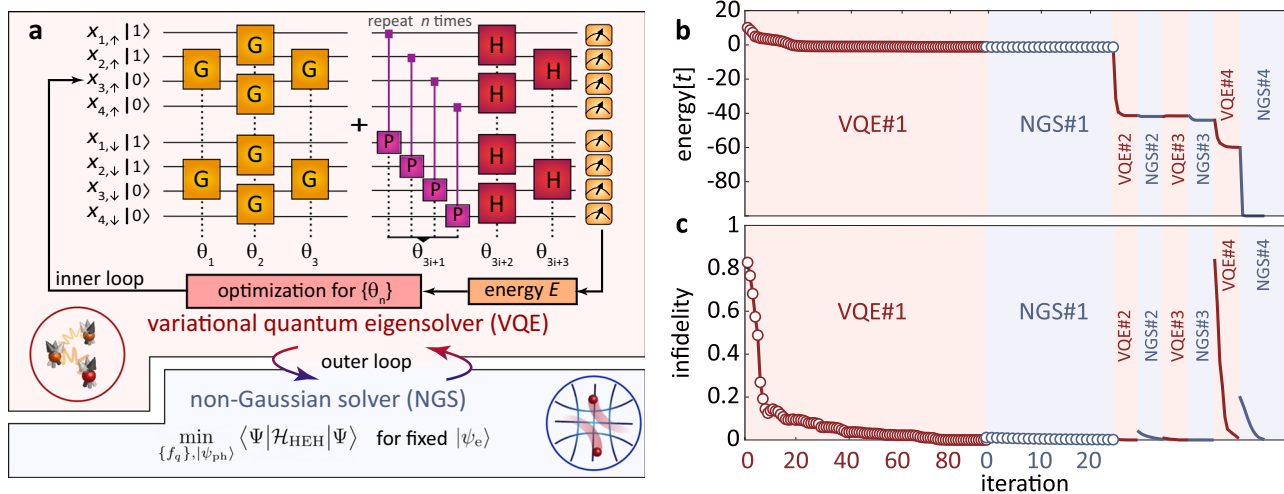

Fig. 1 Hybrid quantum algorithm. a The hybrid quantum algorithm iterates between a variational quantum eigensolver (VQE) for the electronic and a non-Gaussian solver (NGS) for the phonon part of the many-body ground state. The quantum circuit structure for a 4-site example at half filling contains Givens rotations G, on-site gates P, and hopping gates H. The P and H layers are repeated n times to express the ground state wavefunction. Within each layer, gates share the same variational parameters θ_i, which are optimized on a classical computer inside each VQE iteration. **b** Convergence of the NGS-VQE algorithm, reflected by the total energy as a function of inner-loop (NGS or VQE) iteration steps for a 4-site Hubbard-Holstein model with $u = 10$, $\lambda = 10$, and $\omega = 1$. VQE steps were performed with quantum circuit statevector simulations and a circuit depth of $n = 5$. Alternative outer-loop iterations are colored in red (for VQE) and blue (for NGS) and the data points are compressed after NGS #1, for illustration purposes. **c** Convergence of the ground state infidelity $1 − F$ during each iteration. The reference state chosen for each outer-loop iteration was obtained by exact diagonalization on classical computers.

We conclude our analysis by investigating the scaling of the algorithm's performance with respect to the system size, indicating the reduction of exponentially increasing complexity. Moreover, unlike prior studies on EPC systems implemented in trapped ions[47,48], our approach is not limited to a particular hardware platform. This makes our algorithm a promising candidate for studying systems with strong EPCs and electron-electron interactions beyond classically solvable problems.

Results

Variational non-Gaussian VQE (NGS-VQE) method. We consider a prototypical correlated system, where electronic correlations are described by the local Coulomb interaction—the Hubbard model, while electron-phonon coupling follows the linear Fröhlich-type density-displacement interaction. While the latter is usually also simplified into local couplings—the Holstein model—recent experimental discoveries in cuprates have indicated the importance of nonlocal couplings[49–52]. Including all these interactions, we obtain the Hubbard-extended-Holstein (HEH) model, whose Hamiltonian is

$$
\begin{aligned}
\mathcal{H}_{\text{HEH}} &= -t \sum_{\langle i,j \rangle, \sigma} \left(c_{i,\sigma}^\dagger c_{j,\sigma} + \text{h.c.} \right) + U \sum_i n_{i,\uparrow} n_{i,\downarrow} \\
&\quad + \sum_{i,j,\sigma} g_{ij} \left(a_i + a_i^\dagger \right) n_{j,\sigma} + \omega_0 \sum_i a_i^\dagger a_i.
\end{aligned}
\tag{1}
$$

Here, $c_{i,\sigma}$ ($c_{i,\sigma}^\dagger$) annihilates (creates) an electron at site i with spin σ, and a_i ($a_i^\dagger$) annihilates (creates) a phonon at site i; $n_{i,\sigma} = c_{i,\sigma}^\dagger c_{i,\sigma}$ denotes the electron density operator for site i and spin σ. Among the model parameters, t sets the (nearest-neighbor $\langle i,j \rangle$) hopping integral, U sets the on-site repulsive interaction, ω_0 sets the Einstein phonon energy. g_{ij} is the coupling strength between the phonon displacement at site i and electron density at site j. While our method can tackle any distribution of EPCs, as discussed later, we restrict ourselves to local $g = g_{ii}$ and nearest-neighbor coupling $g' = g_{i,i \pm 1}$ in one dimension.

When the EPC is local, i.e., $g_{ij} = g\delta_{ij}$, the HEH model is reduced to the Hubbard-Holstein model. The physical properties of the Hubbard-Holstein model have been studied with various numerical methods, in one-dimensional (1D) systems[53–60], two-dimensional (2D) systems[61–65], and infinite dimensions[66–68]. The phase diagram of the Hubbard-Holstein model is controlled by three dimensionless parameters, notably $u = U/t$ for electronic correlations, $\lambda = g^2/\omega_0 t$ for the effective EPC, and $\omega = \omega_0/t$ for phonon retardation effects. The presence of nonlocal EPCs has been studied recently, motivated by the observed attractive nearest-neighbor interactions in cuprate chains[49]. Due to this reason, numerical studies of the HEH model primarily focused on 1D systems[50,51]. In this paper, we also restrict ourselves to periodic 1D systems, while the presented algorithm can be naturally extended to 2D.

To handle the strongly entangled electronic wavefunction and unbounded phonon Hilbert space simultaneously, we employ a variational non-Gaussian construction of the many-body wavefunction[44,69]. A universal electron-phonon wavefunction can always be written in the form of

$$
|\Psi\rangle = U_{\text{NGS}}(\{f_q\}) |\psi_{\text{ph}}\rangle \otimes |\psi_{\text{e}}\rangle,
\tag{2}
$$

where the right-hand side is a direct product of electron and phonon states (denoted as $|\psi_{\text{e}}\rangle$ and $|\psi_{\text{ph}}\rangle$, respectively), with the variational non-Gaussian transformation $U_{\text{NGS}} = e^{i\mathcal{S}}$ and the (Hermitian) operator $\mathcal{S}$ being a polynomial formed by c, $c^\dagger$, a, and $a^\dagger$ operators (with any sub-indices). The functional class of Eq. (2) is a complete representation of the full electron-phonon Hilbert space. The variational solution based on this approach is

guaranteed to be accurate, provided that $\mathcal{S}$ can assume arbitrary polynomials. The accuracy usually converges at a relatively low order in the exponent[70]. When determining the order of polynomials in $\mathcal{S}$, one should balance theoretical needs and computational feasibility: including high-order powers of electronic and phonon operators in $\mathcal{S}$ improves the accuracy and expands the applicability to complex models; however, these powers also lead to a large variational parameter space and a complex energy representation form. As benchmarked by exact diagonalization (ED) and determinant quantum Monte Carlo (DQMC) simulations of small clusters[45,46], it is sufficient to truncate the $\mathcal{S}$ operator to the lowest-order terms for the Holstein-type coupling [see Eq. (7) in the "Methods" section]. Denoting these lowest-order coefficients as $\{f_q\}$ (q is the quantum number, naturally chosen as momentum for periodic systems), we have the variational non-Gaussian transformation $U_{\text{NGS}}(\{f_q\})$ fully determined by these parameters.

Using this ansatz, we solve the HEH problem by minimizing the average energy

$$
E(\{f_q\}, |\psi_{\text{ph}}\rangle, |\psi_{\text{e}}\rangle) = \langle \Psi | \mathcal{H}_{\text{HEH}} | \Psi \rangle
\tag{3}
$$

self-consistently with respect to the unrestricted electronic state $|\psi_{\text{e}}\rangle$ and the variational parameters in $U_{\text{NGS}}(\{f_q\})$ and $|\psi_{\text{ph}}\rangle$. Within each iteration, the variational non-Gaussian parameters $\{f_q\}$ and the phonon wavefunction $|\psi_{\text{ph}}\rangle$ (here restricted to be a Gaussian state) are optimized using the imaginary-time equations of motion derived in ref. [45] (see Fig. 1a). This is referred to as the non-Gaussian (NGS) solver, whose computational complexity scales polynomially with the system size L. On the other hand, the fully entangled electronic part $|\psi_{\text{e}}\rangle$ of the wavefunction, represented by a tailored quantum circuit, can be obtained by regarding the $|\psi_{\text{ph}}\rangle$ and $\{f_q\}$ as fixed and further minimizing the total energy. The latter step is equivalent to solving the electronic ground state of an effective Hubbard Hamiltonian $\mathcal{H}_{\text{eff}} = \langle \psi_{\text{ph}} | U_{\text{NGS}}^\dagger \mathcal{H}_{\text{HEH}} U_{\text{NGS}} | \psi_{\text{ph}} \rangle$. Physically, this $\mathcal{H}_{\text{eff}}$ describes the behavior of polarons, formed by phonon-dressed electrons. The phonon dressing gives rise to a heavier effective mass by modifying the hopping strength $\tilde{t}$ and mediates a long-ranged attraction $\tilde{V}_{ij} < 0$ between polarons, in the form of Eq. (9) in the "Methods" section. In the case of Holstein couplings, Gaussian states are an efficient representation of the phonon wavefunction $|\psi_{\text{ph}}\rangle$[44,45,69]. Gaussian states allow to represent the effective nearest-neighbor hopping and phonon-mediated interactions in closed-form, as shown in Eqs. (10) and (11) of the "Methods" section (see also ref. [50]).

Within each self-consistent iteration, the key complexity of solving the electron-phonon-coupled problem has thus been converted into solving a purely electronic Hamiltonian $\mathcal{H}_{\text{eff}}$ with extended Hubbard interactions $\tilde{V}_{ij}$. This electronic problem can be efficiently embedded on a quantum hardware by using a suitable fermionic encoding. Here, we employ the Jordan-Wigner transformation, which maps each electron with given spin orientation to one qubit [see "Methods" section]. By applying a set of parameterized rotations to these qubits, we obtain a quantum circuit representing a variational electronic wavefunction $|\psi_{\text{e}}(\{\theta_i\})\rangle$. The self-consistent quantum-classical iterations in VQE then optimize the variational gate parameters $\{\theta_i\}$ to minimize the energy $\langle \psi_{\text{e}}(\{\theta_i\}) | \mathcal{H}_{\text{eff}} | \psi_{\text{e}}(\{\theta_i\}) \rangle$. The solution of VQE approximates $|\psi_{\text{e}}(\{\theta_i\})\rangle$ in the variational ground state of Eq. (2). Unless explicitly specified otherwise, we conduct the VQE step of the NGS-VQE iterations with exact statevector simulations using Qiskit[71].

The standard Hubbard model has been successfully studied with various quantum circuits. Here, we employ the Hamiltonian variational ansatz[72], which can be naturally extended to nonlocal interactions: inspired by the quantum adiabatic theorem, it starts from an efficient encoding of the non-interacting lattice model with translational symmetry[73–76], and then evolves the state using alternating kinetic energy and interacting terms[15,17] [see "Methods" section]. The specific ansatz for the quantum circuit is presented in the upper panel of Fig. 1a. Since the ground state of a finite-size periodic system preserves translational symmetry, we assume the quantum gates in the same layer to share the same parameters (denoted as θ_n in Fig. 1a). The expressibility of the quantum circuit ansatz is controlled by the repetition number n of the evolution block (P and H gates in Fig. 1a). Depending on the hardware specific transpilation, the number of CNOT gates for a given n follows as $6 + 5 \times n$. This quantum circuit represents an efficient encoding if n does not scale exponentially with the system size L. We investigate the scaling with the system size in the "Scaling in circuit depth and system size" subsection, and show that the chosen ansatz leads to a quantitatively accurate performance of the hybrid quantum algorithm.

Figure 1b shows an example of the NGS-VQE simulation for a 4-site Hubbard-Holstein model with $u = 10$ and $\lambda = 10$. Due to the variational nature of each step in the self-consistent NGS-VQE iteration, the total energy E always decreases. Thus, this NGS-VQE iteration is ensured to converge to a local energy minimum within the variational space set by Eq. (2), which provides a good approximation for the ground state. It is worth noting that the energy evolution is not always smooth, where a sudden drop indicates a dramatic change in the variational wavefunction from one phase to another. In the example presented in Fig. 1b, the initial state is prepared by setting the phonon wavefunction to vacuum. Consequently, the first outer-loop iteration with VQE (VQE#1 in the panel) starts with a pure Hubbard model, followed by the adjustment of phonon states and NGS parameters (NGS#1 in the panel). After the entire first outer-loop iteration (VQE#1 and NGS#1), the electronic state $|\psi_e\rangle$ lies in an antiferromagnetic (AFM) state as a solution for the pure Hubbard model, while the phonon state $|\psi_{ph}\rangle$ induces a large attractive potential in the form of Eq. (11) in the "Methods" section. This phonon-mediated interaction tends to stabilize a charge density wave (CDW), which contradicts the AFM state (see discussion in "Charge and spin phases in the Hubbard-Holstein model" for details). As a result, the electronic state rapidly evolves once the second self-consistent iteration (VQE#2) starts.

In addition to the energy evolution, we parameterize the wavefunction error using the infidelity, defined as $1 - F$ with the fidelity $F = \left| \langle \Psi_{VQE} | \Psi_{ED} \rangle \right|^2$. In this context, the reference ground state $|\Psi_{ED}\rangle$ is chosen as the optimal solution for each VQE and NGS step of the outer-loop iteration. Figure 1c shows the convergence of the wavefunction for the same system as Fig. 1b. By comparing these two panels, one can observe that a slow energy evolution may come with a relatively rapid change of wavefunction parameters, indicative of a barren plateau[14]. Therefore, the infidelity may experience significant changes in later (outer-loop) iterations when the energy is close to convergence. We emphasize that the infidelity is posterior and cannot be used as the target function of the iteration.

In contrast to solving a Hubbard model, the NGS-VQE method involves a self-consistent outer loop between electrons and phonons. Thus, the combined NGS-VQE efficiency is essential for optimal results. To mitigate optimization issues of the variational quantum circuit, for instance the barren plateau or a multitude of local minima, we employ a three step optimization. First of all,

since all gates within a single ansatz layer share the same variational parameter θ_i, we can reuse parameters across circuits for different system sizes L. We therefore pre-run the VQE with smaller system sizes to initialize the circuit of the target system with these converged variational parameters. Moreover, the ground state evolves adiabatically for small changes in the model parameters (u, λ, and ω) within the same phase. This is why we further recycle converged parameters if results for similar model parameters exist. Finally, we adaptively adjust the VQE convergence criterion during the outer-loop NGS-VQE iterations by increasing the number of quantum measurements. Since the initial phonon state and variational non-Gaussian parameters are far from saddle points, we start using just a small number of measurements to give a low-accuracy estimation of the electronic ground state; with the progress of NGS-VQE iterations, we gradually raise the convergence criterion for the electronic state. All these strategies help to improve the overall performance and reduce the runtime of the hybrid NGS-VQE algorithm, especially relevant in hardware implementations (see Supplementary Note 1).

Simulating correlated electron-phonon systems

Charge and spin phases in the Hubbard-Holstein model. The Hubbard-Holstein model and its extension set the stage to study the interplay of electronic correlations and EPCs in quantum materials. At half-filling and in 1D, this model results in a rich phase diagram, hosting an AFM, CDW, and a narrow intermediate phase[53–60]. To demonstrate the accuracy and efficiency of the NGS-VQE algorithm, we first restrict ourselves to the pristine Hubbard-Holstein model with $g' = 0$ and simulate the spin and charge structure factors of the ground state for different model parameters. The (static) spin structure factor is defined as

$$S(q) = \sum_{ij} \langle (n_{i\uparrow} - n_{i\downarrow})(n_{j\uparrow} - n_{j\downarrow}) \rangle e^{-iq \cdot (r_i - r_j)} / L, \quad (4)$$

while the (static) charge structure factor is defined as

$$N(q) = \sum_{ij} \langle (n_{i\uparrow} + n_{i\downarrow})(n_{j\uparrow} + n_{j\downarrow}) \rangle e^{-iq \cdot (r_i - r_j)} / L. \quad (5)$$

Using the half-filled system as the benchmark platform in this paper, we focus on the nesting momentum $q = \pi$ for both structure factors. In the regime where electronic interactions dominate ($u \gg \lambda$), the spin structure factor $S(\pi)$ prevails over the charge structure factor, reflecting an AFM state in a finite cluster (see Fig. 2a, b for $\omega = 10$). With the increase of $u - 2\lambda$, $N(\pi)$ gradually vanishes as charge degrees of freedom are frozen with a substantial energy penalty for double occupations. In the other limit where EPCs dominate ($\lambda \gg u$), the charge structure factor $N(\pi)$ prevails over the spin structure factor $S(\pi)$. This reflects the onset of a CDW state, although a more rigorous identification requires either scaling to larger system sizes or excited-state analysis. Physically, the CDW is stabilized by the energy gain through a lattice distortion, forming an alternating pattern of holons and doublons. We summarize the dependence of both spin and charge structure factors on the two interaction parameters in Fig. 2c and d. The trends of these two observables reflect the two dominant phases qualitatively consistent with physical intuition. Due to the underlying finite-size system, the two phases are separated by a crossover instead of a sharp phase boundary. Recent studies have shown the presence of an intermediate Luther-Emery liquid phase for $u \approx 2\lambda$, whose width is controlled by the phonon frequency[60]. The discussion of this phase requires finite-size scaling and is beyond the scope of this paper.

To determine the quantitative accuracy of our hybrid quantum algorithm, we compare the converged ground state for each set of model parameters against the NGSED solutions. The accuracy of the latter has been benchmarked by ED and DQMC[45,46,77]. As
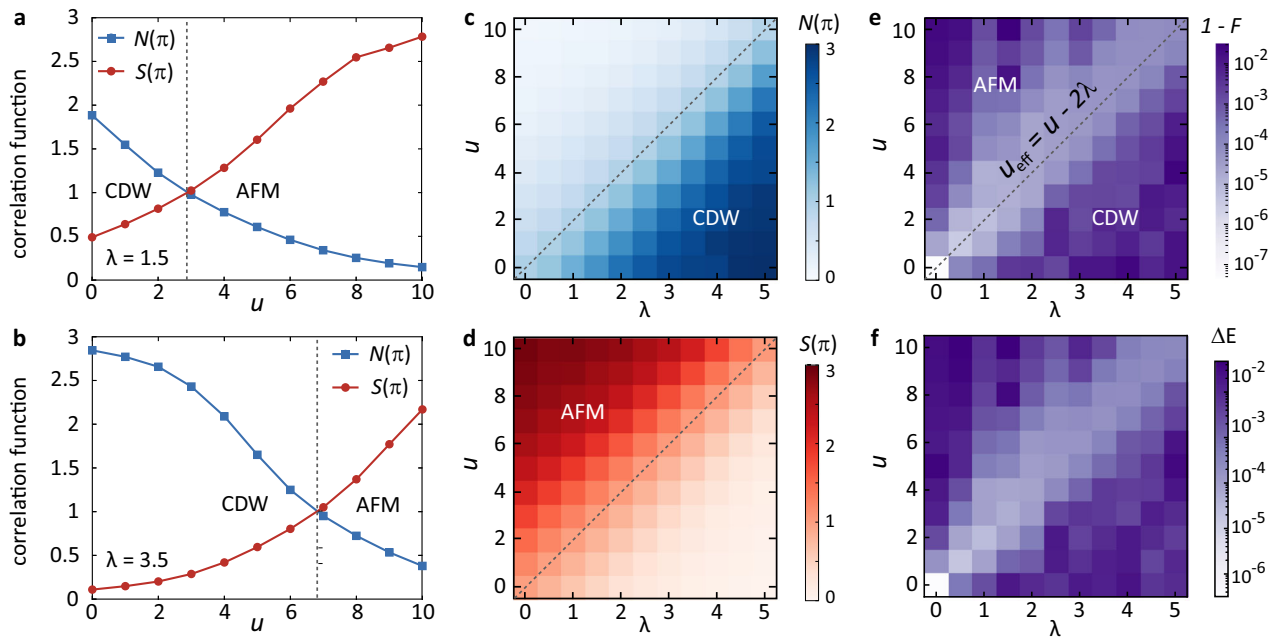
Fig. 2 Phase diagram of the one-dimensional Hubbard-Holstein model. a, b Charge $N(\pi)$ and spin $S(\pi)$ structure factors for the ground state of a 6-site Hubbard-Holstein model, simulated by the non-Gaussian solver variational quantum eigensolver (NGS-VQE) algorithm as a function of u for fixed **a** $\lambda = 1.5$ and **b** $\lambda = 3.5$. The charge-density-wave (CDW) and antiferromagnetic (AFM) regimes are marked. The phonon frequency is set as $\omega = 10$ and the quantum circuit depth is $n = 9$. **c, d** Distribution of the static **c** charge and **d** spin structure factors in the $u - \lambda$ parameter plane, for the same conditions as **a** and **b**. The dashed line indicates the anti-adiabatic phase boundary $u = 2\lambda$ between AFM and CDW. **e** Ground state infidelity and **f** (absolute-value) energy error with respect to ED results for the phase diagram in **c** and **d**.

shown in Fig. 2e, the infidelity map suggests that even the largest error is in the single-digit percentage range, at most 0.03. These errors do not change significantly with increasing system size, as outlined in the "Scaling in circuit depth and system size" subsection. Interestingly, the most accurate solutions (with infidelity of order 10^{-5}) are obtained near the boundary of the CDW and AFM phases, i.e., along the diagonal $u \approx 2\lambda$. In this regime, the finite-system solution is more metallic, due to the delicate balance between the electronic repulsion and phonon-mediated attraction. Therefore, the true ground state of systems near the phase boundary can be efficiently captured with a Slater determinant prepared by Givens rotations[73-76]. In contrast, the infidelity increases when the system evolves into CDW or AFM states, although the NGS-VQE algorithm yields quantitatively accurate results throughout the phase diagram. This observation is contrasting the intuition that the AFM or CDW states are more classical. Instead, these states are cat states in these small and low-dimensional systems. An accurate representation of these highly-entangled states with long-range correlations, therefore, requires deeper quantum circuits and, accordingly, more gates. The dependence on circuit depth will be discussed in the "Scaling in circuit depth and system size" subsection. This sensitivity of the simulation accuracy to the model parameters is also reflected by the error of the ground-state energy, as shown in Fig. 2f.

Up to now, the benchmark has been conducted with relatively large phonon frequencies $\omega = 10$, where the competition between CDW and AFM states is primarily controlled by the effective local interaction $u_{\text{eff}} = u - 2\lambda$ after integrating phonon fields. However, phonon frequencies in typical correlated materials are usually comparable to the electronic bandwidth, if not even reaching the adiabatic limit ($\omega \to 0$). The dependence of charge and structure factors on different phonon frequencies is discussed in Supplementary Note 2. In the thermodynamic limit, smaller phonon frequencies usually lead to a steeper crossover between

the two phases[54-57], with both $S(\pi)$ and $N(\pi)$ dropping more rapidly when approaching the phase boundary. Note, however, that this intermediate phase cannot be resolved in a small cluster.

Phonon-mediated interactions in the Hubbard-extended-Holstein model. The wavefunction ansatz in Eq. (2) allows to extract the effective model $\mathcal{H}_{\text{eff}}$ in the polaronic basis while solving for the ground state. This approach has been used to quantify the recently discovered nearest-neighbor electronic attraction $\tilde{V}$ in cuprate chains[50]. Here, we evaluate $\tilde{V}$ for different systems using the NGS-VQE algorithm both to provide intuition about phonon-mediated interactions in different limits and to benchmark the validity of the method under different conditions.

We first examine the Hubbard-Holstein model without g'. Figure 3a, c and b, d shows the simulated local and nearest-neighbor attractive interaction in the polaronic basis. Since this interaction was discovered in cuprates with strong electron correlations, we restrict ourselves to the AFM regime ($u \gg \lambda$) and set $\lambda = 1$. In the anti-adiabatic limit, the local interaction $\tilde{V}_{ii}$ asymptotically approaches $-\lambda = -1$ and all nonlocal interactions $\tilde{V}_{i \neq j}$ vanish (see Fig. 3c, d). This is consistent with the integration of phonons in field theory. With the decrease of ω and proximity to u, Coulomb interactions start to influence the distribution of $\tilde{V}_{ij}$. Such an influence is more obvious for large u, where the electronic correlations are strong and renormalize the phonon self-energy. This effect can be captured by the wavefunction ansatz of Eq. (8). The electron-dressing effect for the phonon self-energy is described by Ω_{eff} in ref. [45]. Simultaneously, the retardation effect of finite-frequency phonons mediates the effective interaction at finite distance. Therefore, the effective nearest-neighbor attraction $\tilde{V}_{i,i+1}$ increases for lower phonon frequencies (see Fig. 3b, d).

With further decreasing phonon frequencies, the impact of phonons becomes a mean-field-like deformation potential instead
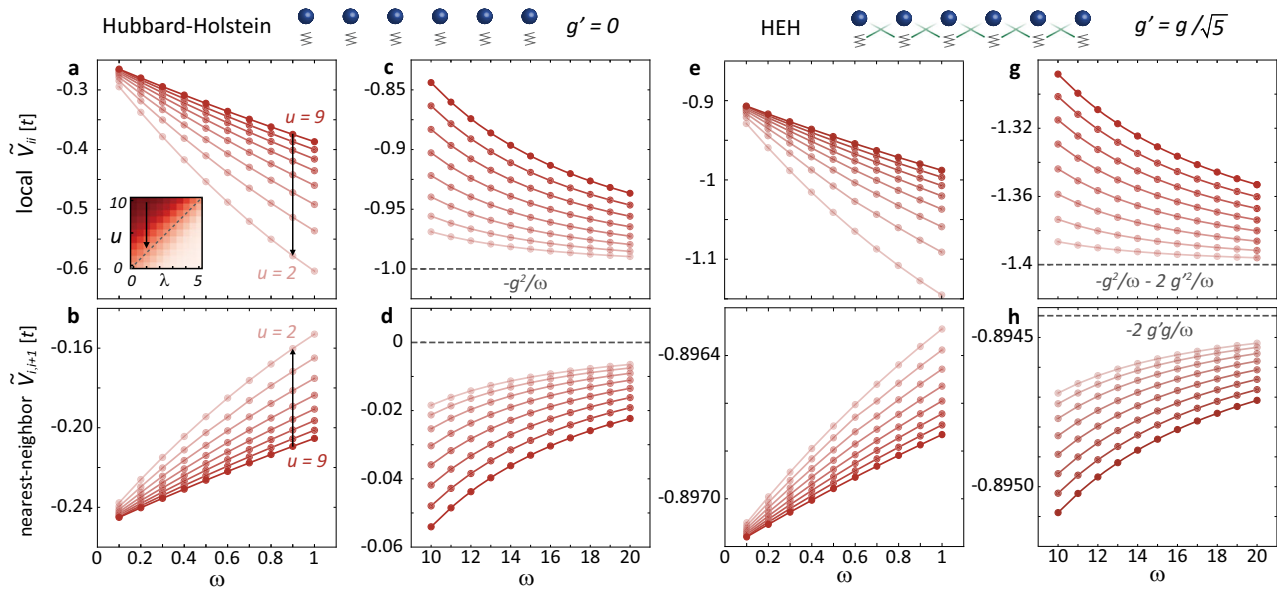
Fig. 3 Phonon-mediated interactions for the ground state of the Hubbard-Holstein and Hubbard-Extended-Holstein (HEH) model. a, b Local ($r = 0$) and nearest-neighbor ($r = 1$) interaction strengths $\tilde{V}$ for various Hubbard u values within the antiferromagnetic (AFM) phase ($g' = 0$, $\lambda = 1$) and small phonon frequencies (close to the adiabatic limit). The inset in **a** highlights the considered path in the phase diagram (black arrow). **c, d** Local ($r = 0$) and nearest-neighbor ($r = 1$) interaction strengths $\tilde{V}$ for the same interaction parameters as **a** and **b**, but with large phonon frequencies. The dashed lines suggest the asymptotic values in the anti-adiabatic limit. **e–h** Local ($r = 0$) and nearest-neighbor ($r = 1$) interaction strengths $\tilde{V}$ for the same conditions as (**a–d**), but for the extended Hubbard model with $g' = g/\sqrt{5}$. Similarly, the dashed lines in **g** and **h** indicate the asymptotic values in the anti-adiabatic limit.

of a virtual process. Such a deformation potential contributes as an overall chemical potential instead of media of a two-particle interaction. Therefore, the simulated $\tilde{V}_{ij}$ becomes extremely nonlocal and evolves into an all-to-all interaction, which is equivalent to a chemical potential shift in a canonical ensemble with fixed particle number. In the $\omega \to 0$ limit, phonon-mediated interactions are insensitive to the Hubbard u, because the mean-field phonon distortion is determined only by the average local electron density, which is approximately fixed in the AFM phase (see Fig. 3a, b). This insensitivity is similar to the anti-adiabatic limit but has a different origin.

We now move on to discuss the impact of nearest-neighbor EPC g' on the complexity and accuracy of the hybrid quantum algorithm. We fix the ratio $g'/g = 1/\sqrt{5}$ to reflect the geometric relation of apical oxygens in a 1D transition-metal oxide[50]. With electrons coupled to their nearest-neighbor phonons directly, the mediation of $\tilde{V}_{i,i+1}$ can be generated without retardation effect. Therefore, the asymptotic $\tilde{V}_{i,i+1}$ in the anti-adiabatic limit is no longer zero but acquires a finite value (see Fig. 3h). This asymptotic interaction strength can be analytically calculated as $-2gg'/\omega$, which is more evident than the additional interactions caused by retardation effects (the latter is three orders of magnitude smaller than the former). At the same time, the phonon-mediated local interaction $\tilde{V}_{ii}$ is further strengthened by this nonlocal g' coupling. The anti-adiabatic value of $\tilde{V}_{ii}$ approaches $-g^2/\omega - 2g'^2/\omega$ (see Fig. 3g). Due to the geometric distance controlling g'/g, the strength of $\tilde{V}_{ii}$ is still comparable to that of the Hubbard-Holstein model ($g' = 0$). In the adiabatic limit, the effective interactions are similar to those obtained from the Hubbard-Holstein model, asymptotically approaching an extremely delocalized $\tilde{V}_{ij}$. Compared to the $g' = 0$ case (Fig. 3a, b), the only difference is the asymptotic value when ω approaches zero. Using the fact that, in the long-wavelength limit ($q = 0$), $\tilde{V}$ is proportional to g_q^2/ω and $g_q = g + 2g' \cos q$, we can estimate the ratio between these two asymptotic $\tilde{V}_{ij}$ values (for $g' = g/\sqrt{5}$

and $g' = 0$) to be $(1 + 2/\sqrt{5})^2 \approx 3.59$. This ratio agrees with the simulated results in Fig. 3a, b, e, and f.

Scaling in circuit depth and system size. The results presented in Fig. 3 demonstrate that our hybrid quantum algorithm is able to produce quantitatively accurate results across the full phonon spectrum (see Supplementary Note 2 for a comparison to NGSED results). To further analyze the accuracy of our algorithm, we investigate the influence of different system sizes L. The depth of the quantum circuit controls the expressibility of the variational state, potentially allowing for a more accurate approximation of the electronic ground state by increasing n. However, an efficient encoding on quantum computing platforms is only possible if the depth of the employed quantum circuit does not scale exponentially with the system size L. As shown in Fig. 4a, the ground states for small-u systems can be efficiently expressed by a Slater determinant. Thus, only a few layers are needed to reach ground state energy errors below 1×10^{-6} when compared to ED. Larger u, however, requires deeper circuits, reaching a plateau of errors of the order 10^{-4} to 10^{-5} in the ground state energy. In order to investigate the scaling of necessary n with the system size L, we consider a fixed error in the electron ground state energy of $|E_{\text{NGS-VQE}} - E_{\text{ED}}|/L = 0.1t$. The circuit depth required to achieve this performance as a function of L is shown in Fig. 4b, highlighting a moderate increase in depth for small and large u. Intermediate values for u, however, require significantly deeper circuits, as quantum fluctuations are larger around the crossover between metallic and AFM phase.

So far, we have considered the influence of finite-depth quantum circuits on the electronic part of the many-body ground state. The hybrid NGS-VQE algorithm combines the electron solver with a variational NGS solver for the phonon and non-Gaussian components. That being said, errors in the VQE solutions do not necessarily accumulate, but can actually be mitigated by the phonon solver. Considering again a fixed error in the electron ground-state energy of $|E_{\text{NGS-VQE}} - E_{\text{ED}}|/L = 0.1t$
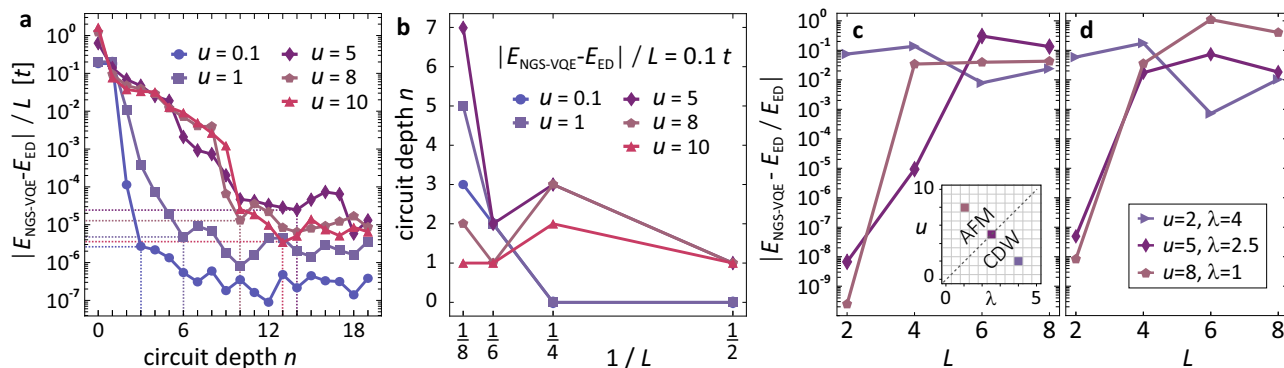
Fig. 4 Scaling behavior of the hybrid quantum algorithm. a Simulation error for the ground-state energy $E_{\text{NGS-VQE}}$ of the employed quantum circuit ansatz as a function of circuit depth n and various on-site interactions u, compared to ED ($\lambda = 0$). This circuit depth n follows the definition in Fig. 1a for a 6-site Hubbard model. **b** Scaling of circuit depth n with system size L for a fixed accuracy of $|E_{\text{NGS-VQE}} - E_{\text{ED}}|/L = 0.1t$ and various on-site interactions u ($\lambda = 0$). The required circuit depth changes only slightly with the system size for small and large values of u. **c** Relative error of the converged ground-state energy for three distinct parameter sets for the Hubbard-Holstein model as a function of system size L [the inset highlights the charge density wave (CDW) and antiferromagnetic (AFM) phase]. The phonon frequency is $\omega = 10$ and the variational quantum eigensolver (VQE) was performed with the circuit depth obtained in panel **b**. The error remains approximately constant when increasing L from 4 to 8. **d** Same as panel **c**, but for a small phonon frequency $\omega = 1$.

and corresponding circuit depth n, we investigate the accuracy of the hybrid quantum algorithm in different regions of the phase diagram. Specifically, we consider the relative error in the ground-state energy of the converged extended-Hubbard Hamiltonian [see Eq. (9)], containing the phonon dressing of kinetic hopping and long-range interactions. Figure 4c, d indicates that the NGS-VQE simulation errors are usually at least an order of magnitude smaller than those of the electronic solvers. The largest errors are obtained for small phonon frequencies (Fig. 4d, $\omega = 1$), where the absence of quantum fluctuations hinders the phonon solver to escape local minima during the self-consistent iteration[45]. Warm-up iterations with larger phonon frequencies can help to alleviate this issue[45]. Moreover, the relative errors do not increase for systems larger than $L = 4$, indicating quantitatively accurate results across different system sizes and phases. The only exception appears in the CDW phase at small phonon frequencies such as $\omega = 1$, where the relative error oscillates with L, likely due to the degeneracy of ground states. The ability to mitigate errors of the quantum solver also provides a promising path to experimental realizations. Hardware implementations, irrespective of the specific platform, suffer from decoherence[78], making noise resilient algorithms of key importance. Our hybrid quantum algorithm is able to improve VQE results over a wide range of phonon frequencies, phase regions, and noise levels, suggesting efficient hardware realizations (see Supplementary Note 3).

Conclusions

Our NGS-VQE method provides a general framework for performing accurate and efficient quantum simulations of electron-phonon systems with arbitrary interaction strengths. Using this method, we have studied the Hubbard-Holstein and HEH models as examples, reproduced the CDW-AFM crossover with high precision, and extracted the phonon-mediated interactions in a wide range of phonon frequencies. While we focused on paradigmatic (and experimentally relevant) cases, this method can be generally applied to any model with electronic Coulomb correlations and Fröhlich-type electron-phonon couplings. The commutation between the NGS transformation [$e^{i\mathcal{S}}$ with $\mathcal{S}$ defined in the form of Eq. (7) of the "Methods"] guarantees a closed-form effective Hamiltonian similar to Eq. (9). This hybrid algorithm can be extended to other types of electron-boson interactions (like the Su-Schrieffer-Heeger phonon and cavity QED) through

the generalization of the non-Gaussian transformation U_{NGS} and its optimization strategy. Anharmonic potentials can be tackled at the price of replacing $\left|\psi_{\text{ph}}\right\rangle$ by more complicated many-body wavefunctions similar to the electronic ones. Both generalizations are accompanied by the increase of computational complexity and should be designed based on the requirements of specific models. Moreover, as demonstrated in ref. [46], this framework can be extended to non-equilibrium dynamics, which requires a reliable quantum solver for the long-time propagation of $\left|\psi_e\right\rangle$. The Fourier transform of non-equilibrium dynamics with two- or multi-time correlation functions further paves the way to excited-state spectra[79–81].

Our work shows that the phonon solver can mitigate potential errors of the quantum hardware, facilitating a future experimental implementation. The success of an experimental realization, how-ever, relies on an efficient implementation of the required quantum circuits, respecting the connectivity of a given device. This is especially the case for nonlocal gates, like the P gates of our ansatz representing electron-electron interactions. Trapped ion and cold atom-based platforms offer high qubit-connectivities[82], reducing potential swap-overheads when implementing entangling gate-layers such as the P and H gates in our ansatz. Superconducting systems, on the other hand, have a more limited qubit-connectivity but operate at much faster rates, making them favorable for two-level NGS-VQE iterative schemes. Therefore, practical implementations of the algorithm proposed in this study call for developing higher-connectivity superconducting hardware or error mitigation schemes to compensate for potential swap-overheads.

Methods

NGS-VQE method and effective Hamiltonian. As mentioned in the main text, the variational electron-phonon wavefunction in the NGS-VQE method is given as

$$|\Psi\rangle = U_{\text{NGS}}(\{f_q\})\left|\psi_{\text{ph}}\right\rangle \otimes \left|\psi_e\right\rangle, \quad (6)$$

with the non-Gaussian transformation $U_{\text{NGS}} = e^{i\mathcal{S}}$. As bench-marked by ED and DQMC on small clusters[45,46], it is sufficient to truncate the $\mathcal{S}$ operator to the lowest-order terms

$$\mathcal{S}(\{f_q\}) = -\frac{1}{\sqrt{L}}\sum_{qi\sigma}f_q e^{iqx_i}(a_q - a^\dagger_{-q})n_{i,\sigma}, \quad (7)$$

where we use the momentum-space electron density $\rho_q = \sum_{i,\sigma} n_{i,\sigma} e^{-iqx_i}$, and the phonon momentum operator $p_q = i\sum_i(a_i^\dagger - a_i)e^{-iqx_i}/\sqrt{L}$.

The goal of the NGS-VQE solver is to minimize the total energy in Eq. (3) in the variational parameter space spanned by $\{f_q\}$, $|\psi_{ph}\rangle$, and $|\psi_e\rangle$. Without considering anharmonicity, the phonon state to the right of U_{NGS} should be weakly entangled and can be efficiently captured by variational Gaussian states

$$|\psi_{ph}\rangle = e^{-\frac{1}{2}R_0^T \sigma_y \Delta_R} e^{-i\frac{1}{4}\sum_q R_q^\dagger \xi_q R_q}|0\rangle = U_{GS}|0\rangle. \quad (8)$$

Here, Δ_R, ξ_q are variational parameters and $R_q = (x_q, p_q)^T$ denotes the bosonic quadrature notation with canonical position x_q and momentum p_q, where we adopt the reciprocal representation for the phonon displacement $x_q = \sum_j(a_j + a_j^\dagger)e^{-iqr_j}/\sqrt{L}$. For convenience, we parameterize the phonon state using the linearization of U_{GS} named S_q, which satisfies $U_{GS}^\dagger(x_q, p_q)^T U_{GS} = S_q(x_q, p_q)^T$. The NGS-VQE method minimizes the total energy by updating $|\psi_e\rangle$ and $|\psi_{ph}\rangle$ iteratively.

With fixed U_{NGS} and $|\psi_{ph}\rangle$, the electronic problem that the quantum machine has to solve is the ground state of an effective Hamiltonian

$$\begin{aligned}\mathcal{H}_{eff} = &-\tilde{t}\sum_{\langle i,j\rangle,\sigma}\left(c_{i,\sigma}^\dagger c_{j,\sigma} + \text{h.c.}\right) + U\sum_i n_{i,\uparrow}n_{i,\downarrow}\\ &+\sum_{i,j}\sum_{\sigma,\sigma'}\tilde{V}_{ij}n_{i,\sigma}n_{j,\sigma'} + \tilde{E}_{ph},\end{aligned} \quad (9)$$

where $\tilde{E}_{ph} = \frac{1}{4}\omega\sum_q\left(\text{Tr}[S_q S_q^\dagger] - 2\right)$. The phonon-dressed hopping becomes

$$\tilde{t} = t e^{-\sum_q f_q^2(1-\cos q)e_2^T S_q S_q^\dagger e_2/L}, \quad (10)$$

and the effective interaction is

$$\tilde{V}_{ij} = \frac{1}{L}\sum_q\left[2\omega_0 f_q^2 - 4g_q f_q\right]e^{iq(r_i-r_j)}. \quad (11)$$

The VQE solution of the effective Hamiltonian in Eq. (9) gives $|\psi_e\rangle$ in Eq. (6). The iterative optimization of U_{NGS} and $|\psi_{ph}\rangle$, for fixed $|\psi_e\rangle$, follows the imaginary time evolution in ref. [45]. It is worth noting that the charge density correlation functions $\langle\rho_q\rho_{-q}\rangle \propto \sum_{ij}\sum_{\sigma\sigma'}n_{i,\sigma}n_{j,\sigma'}$ necessary for the imaginary time evolution of $|\psi_{ph}\rangle$ appear in $\mathcal{H}_{eff}$ as well. They are therefore already measured with the energy expectation value during VQE and result in no additional computational cost.

Quantum circuit and ansatz. To represent the effective Hamiltonian in Eq. (9) on a quantum computer, we rely on the Jordan-Wigner transformation: each electron with given spin orientation is mapped to one qubit. Specifically, it reads

$$S_{i,\sigma}^+ = c_{i,\sigma}^\dagger e^{i\pi\sum_{l<i}n_{l,\sigma}}, \quad (12)$$

$$S_{i,\sigma}^- = c_{i,\sigma} e^{-i\pi\sum_{l<i}n_{l,\sigma}}, \quad (13)$$

where the phase factors retain the fermionic anti-commutation in the spin operators S. Transforming the effective model described by Eq. (9) with L sites then yields $2L$ spin operators. Consequently, a quantum ansatz for the electronic ground state contains $2L$ qubits, which represent occupied $|1\rangle = c^\dagger|0\rangle$ or unoccupied $|0\rangle$ fermionic states. As the effective Hamiltonian preserves occupation number and total spin, we can restrict the electron occupation to half-filling and total spin to zero. Correspondingly, we arrange the qubits representing the two spin

orientations separately (see Fig. 1a), and require that gates connecting the two spin sectors cannot change their respective occupation.

As outlined in the main text, the employed quantum circuit is based on the Hamiltonian variational ansatz[72]. To encode the non-interacting ($U = 0$, $V_{ij} = 0$) electronic model, a sequence of Givens rotations $G(\theta)$, parametrized by θ, is applied to adjacent qubits[73–76]. In the basis $|00\rangle, |01\rangle, |10\rangle, |11\rangle$, the gate is defined as

$$G(\theta) = \begin{pmatrix} 1 & 0 & 0 & 0\\ 0 & \cos\frac{\theta}{2} & -\sin\frac{\theta}{2} & 0\\ 0 & \sin\frac{\theta}{2} & \cos\frac{\theta}{2} & 0\\ 0 & 0 & 0 & 1\end{pmatrix}. \quad (14)$$

The ground state of the full effective model is then obtained by an adiabatic evolution with the Hubbard-like Hamiltonian[15,17]. It can be decomposed into kinetic hopping terms,

$$H(\theta) = e^{-i(c_i^\dagger c_{i+1}+c_{i+1}^\dagger c_i)\theta} = e^{-i(X_iX_{i+1}+Y_iY_{i+1})\theta/2}, \quad (15)$$

in the basis $|00\rangle, |01\rangle, |10\rangle, |11\rangle$ represented as

$$H(\theta) = \begin{pmatrix} 1 & 0 & 0 & 0\\ 0 & \cos\frac{\theta}{2} & -i\sin\frac{\theta}{2} & 0\\ 0 & -i\sin\frac{\theta}{2} & \cos\frac{\theta}{2} & 0\\ 0 & 0 & 0 & 1\end{pmatrix}, \quad (16)$$

and on-site interactions

$$P(\theta) = e^{-in_i n_j\theta} = e^{-i|11\rangle\langle11|_{ij}\theta}, \quad (17)$$

described by

$$P(\theta) = \begin{pmatrix} 1 & 0 & 0 & 0\\ 0 & 1 & 0 & 0\\ 0 & 0 & 1 & 0\\ 0 & 0 & 0 & e^{i\theta}\end{pmatrix}. \quad (18)$$

The alternating sequence of phase gates (P) and hopping gates (H) is then repeated for a number of repetitions n, controlling the expressibility of the variational ansatz.

Data availability

Code availability

References
1. Keimer, B., Kivelson, S., Norman, M., Uchida, S. & Zaanen, J. From quantum matter to high-temperature superconductivity in copper oxides. *Nature* **518**, 179 (2015).
2. Peruzzo, A. et al. A variational eigenvalue solver on a photonic quantum processor. *Nat. Commun.* **5**, 4213 (2014).
3. Yung, M.-H. et al. From transistor to trapped-ion computers for quantum chemistry. *Sci. Rep.* **4**, 3589 (2014).
4. Farhi, E., Goldstone, J. & Gutmann, S. A quantum approximate optimization algorithm. Preprint at https://arxiv.org/abs/1411.4028 (2014).
5. Moll, N. et al. Quantum optimization using variational algorithms on near-term quantum devices. *Quantum Sci. Technol.* **3**, 030503 (2018).

6. Endo, S., Cai, Z., Benjamin, S. C. & Yuan, X. Hybrid quantum-classical algorithms and quantum error mitigation. *J. Phys. Soc. Jpn.* **90**, 032001 (2021).

7. Cerezo, M. et al. Variational quantum algorithms. *Nat. Rev. Phys.* **3**, 625 (2021).

8. Bharti, K. et al. Noisy intermediate-scale quantum algorithms. *Rev. Mod. Phys.* **94**, 015004 (2022).

9. Kandala, A. et al. Hardware-efficient variational quantum eigensolver for small molecules and quantum magnets. *Nature* **549**, 242 (2017).

10. Colless, J. I. et al. Computation of molecular spectra on a quantum processor with an error-resilient algorithm. *Phys. Rev. X* **8**, 011021 (2018).

11. Takeshita, T. et al. Increasing the representation accuracy of quantum simulations of chemistry without extra quantum resources. *Phys. Rev. X* **10**, 011004 (2020).

12. Motta, M. et al. Determining eigenstates and thermal states on a quantum computer using quantum imaginary time evolution. *Nat. Phys.* **16**, 205 (2020).

13. Ollitrault, P. J. et al. Quantum equation of motion for computing molecular excitation energies on a noisy quantum processor. *Phys. Rev. Research* **2**, 043140 (2020).

14. Uvarov, A., Biamonte, J. D. & Yudin, D. Variational quantum eigensolver for frustrated quantum systems. *Phys. Rev. B* **102**, 075104 (2020).

15. Cade, C., Mineh, L., Montanaro, A. & Stanisic, S. Strategies for solving the Fermi-Hubbard model on near-term quantum computers. *Phys. Rev. B* **102**, 235122 (2020).

16. Suchsland, P., Barkoutsos, P. K., Tavernelli, I., Fischer, M. H. & Neupert, T. Simulating a ring-like Hubbard system with a quantum computer. *Phys. Rev. Res.* **4**, 013165 (2022).

17. Stanisic, S. et al. Observing ground-state properties of the Fermi-Hubbard model using a scalable algorithm on a quantum computer. *Nat. Commun.* **13**, 5743 (2022).

18. Scalapino, D., Loh Jr, E. & Hirsch, J. d-Wave pairing near a spin-density-wave instability. *Phys. Rev. B* **34**, 8190 (1986).

19. Gros, C., Joynt, R. & Rice, T. Superconducting instability in the large-U limit of the two-dimensional Hubbard model. *Z. Phys. B Condens. Matter* **68**, 425 (1987).

20. Shen, K. et al. Missing quasiparticles and the chemical potential puzzle in the doping evolution of the cuprate superconductors. *Phys. Rev. Lett.* **93**, 267002 (2004).

21. Lanzara, A. et al. Evidence for ubiquitous strong electron-phonon coupling in high-temperature superconductors. *Nature* **412**, 510 (2001).

22. Reznik, D. et al. Electron-phonon coupling reflecting dynamic charge inhomogeneity in copper oxide superconductors. *Nature* **440**, 1170 (2006).

23. He, Y. et al. Rapid change of superconductivity and electron-phonon coupling through critical doping in Bi-2212. *Science* **362**, 62 (2018).

24. Kang, J. & Vafek, O. Strong coupling phases of partially filled twisted bilayer graphene narrow bands. *Phys. Rev. Lett.* **122**, 246401 (2019).

25. Hejazi, K., Liu, C., Shapourian, H., Chen, X. & Balents, L. Multiple topological transitions in twisted bilayer graphene near the first magic angle. *Phys. Rev. B* **99**, 035111 (2019).

26. Guinea, F. & Walet, N. R. Electrostatic effects, band distortions, and superconductivity in twisted graphene bilayers. *Proc. Natl Acad. Sci.* **115**, 13174 (2018).

27. Lian, B., Wang, Z. & Bernevig, B. A. Twisted bilayer graphene: a phonon-driven superconductor. *Phys. Rev. Lett.* **122**, 257002 (2019).

28. Wu, F., MacDonald, A. H. & Martin, I. Theory of phonon-mediated superconductivity in twisted bilayer graphene. *Phys. Rev. Lett.* **121**, 257001 (2018).

29. Peltonen, T. J., Ojajärvi, R. & Heikkilä, T. T. Mean-field theory for superconductivity in twisted bilayer graphene. *Phys. Rev. B* **98**, 220504 (2018).

30. Fausti, D. et al. Light-induced superconductivity in a stripe-ordered cuprate. *Science* **331**, 189 (2011).

31. Hu, W. et al. Optically enhanced coherent transport in $YBa_2Cu_3O_{6.5}$ by ultrafast redistribution of interlayer coupling. *Nat. Mater.* **13**, 705 (2014).

32. Boschini, F. et al. Collapse of superconductivity in cuprates via ultrafast quenching of phase coherence. *Nat. Mater.* **17**, 416 (2018).

33. Rösch, O. & Gunnarsson, O. Electron-phonon interaction in the $t-J$ Model. *Phys. Rev. Lett.* **92**, 146403 (2004).

34. Khatami, E., Macridin, A. & Jarrell, M. Effect of long-range hopping on T_c in a two-dimensional Hubbard-Holstein model of the cuprates. *Phys. Rev. B* **78**, 060502 (2008).

35. Wang, Y., Chen, C.-C., Moritz, B. & Devereaux, T. Light-enhanced spin fluctuations and d-wave superconductivity at a phase boundary. *Phys. Rev. Lett.* **120**, 246402 (2018).

36. Murakami, Y., Werner, P., Tsuji, N. & Aoki, H. Ordered phases in the Holstein-Hubbard model: interplay of strong Coulomb interaction and electron-phonon coupling. *Phys. Rev. B* **88**, 125126 (2013).

37. Kemper, A. F., Sentef, M. A., Moritz, B., Freericks, J. K. & Devereaux, T. P. Direct observation of Higgs mode oscillations in the pump-probe photoemission spectra of electron-phonon mediated superconductors. *Phys. Rev. B* **92**, 224517 (2015).

38. Sentef, M. A., Kemper, A. F., Georges, A. & Kollath, C. Theory of light-enhanced phonon-mediated superconductivity. *Phys. Rev. B* **93**, 144506 (2016).

39. Babadi, M., Knap, M., Martin, I., Refael, G. & Demler, E. Theory of parametrically amplified electron-phonon superconductivity. *Phys. Rev. B* **96**, 014512 (2017).

40. Macridin, A., Spentzouris, P., Amundson, J. & Harnik, R. Electron-phonon systems on a universal quantum computer. *Phys. Rev. Lett.* **121**, 110504 (2018).

41. Li, W. et al. Efficient quantum simulation of electron-phonon systems by variational basis state encoder. *Phys. Rev. Res.* **5**, 023046 (2023).

42. Macridin, A., Spentzouris, P., Amundson, J. & Harnik, R. Digital quantum computation of Fermion-Boson interacting systems. *Phys. Rev. A* **98**, 042312 (2018).

43. Pavošević, F. & Flick, J. Polaritonic unitary coupled cluster for quantum computations. *J. Phys. Chem. Lett.* **12**, 9100 (2021).

44. Shi, T., Demler, E. & Cirac, J. I. Variational study of fermionic and bosonic systems with non-Gaussian states: theory and applications. *Ann. Phys.* **390**, 245 (2018).

45. Wang, Y., Esterlis, I., Shi, T., Cirac, J. I. & Demler, E. Zero-temperature phases of the two-dimensional Hubbard-Holstein model: a non-Gaussian exact diagonalization study. *Phys. Rev. Res.* **2**, 043258 (2020).

46. Wang, Y., Shi, T. & Chen, C.-C. Fluctuating nature of light-enhanced d-wave superconductivity: a time-dependent variational non-Gaussian exact diagonalization study. *Phys. Rev. X* **11**, 041028 (2021).

47. Casanova, J. et al. Quantum simulation of quantum field theories in trapped ions. *Phys. Rev. Lett.* **107**, 260501 (2011).

48. Mezzacapo, A., Casanova, J., Lamata, L. & Solano, E. Digital quantum simulation of the Holstein model in trapped ions. *Phys. Rev. Lett.* **109**, 200501 (2012).

49. Chen, Z. et al. Anomalously strong near-neighbor attraction in doped 1D cuprate chains. *Science* **373**, 1235 (2021).

50. Wang, Y., Chen, Z., Shi, T., Moritz, B. & Devereaux, T. P. Phonon-mediated long-range attractive interaction in one-dimensional cuprates. *Phys. Rev. Lett.* **127**, 197003 (2021).

51. Tang, T., Moritz, B., Peng, C., Shen, Z.-X. & Devereaux, T. P. Traces of electron-phonon coupling in one-dimensional cuprates. *Nat. Commun.* **14**, 3129 (2023).

52. Wang, H.-X., Wu, Y.-M., Jiang, Y.-F. & Yao, H., Spectral properties of 1D extended Hubbard model from bosonization and time-dependent variational principle: applications to 1D cuprate. Preprint at https://arxiv.org/abs/2211.02031 (2022).

53. Hotta, T. & Takada, Y. Unconventional Superconductivity in the Hubbard-Holstein Model. *Phys. B: Condens. Matter* **230**, 1037 (1997).

54. Fehske, H. et al. Peierls-insulator Mott-insulator transition in 1D. *Phys. B: Condens. Matter* **312**, 562 (2002).

55. Fehske, H., Kampf, A. P., Sekania, M. & Wellein, G. Nature of the Peierls-to-Mott-insulator transition in 1D. *Eur. Phys. J. B-Condens. Matter Complex Syst.* **31**, 11 (2003).

56. Tezuka, M., Arita, R. & Aoki, H. Phase diagram for the one-dimensional Hubbard-Holstein model: a density-matrix renormalization group study. *Phys. Rev. B* **76**, 155114 (2007).

57. Fehske, H., Hager, G. & Jeckelmann, E. Metallicity in the half-filled Holstein-Hubbard model. *Eur. Phys. Lett.* **84**, 57001 (2008).

58. Ejima, S. & Fehske, H. Dmrg analysis of the SDW-CDW crossover region in the 1D half-filled Hubbard-Holstein model, in *Journal of Physics: Conference Series*, Vol. 200, 012031 (IOP Publishing, 2010).

59. Clay, R. & Hardikar, R. Intermediate phase of the one dimensional half-filled Hubbard-Holstein model. *Phys. Rev. Lett.* **95**, 096401 (2005).

60. Greitemann, J., Hesselmann, S., Wessel, S., Assaad, F. & Hohenadler, M. Finite-size effects in Luther-Emery phases of Holstein and Hubbard models. *Phys. Rev. B* **92**, 245132 (2015).

61. Nowadnick, E., Johnston, S., Moritz, B., Scalettar, R. & Devereaux, T. Competition between antiferromagnetic and charge-density-wave order in the half-filled Hubbard-Holstein model. *Phys. Rev. Lett.* **109**, 246404 (2012).

62. Nowadnick, E., Johnston, S., Moritz, B. & Devereaux, T. Renormalization of spectra by phase competition in the half-filled Hubbard-Holstein model. *Phys. Rev. B* **91**, 165127 (2015).

63. Karakuzu, S., Tocchio, L. F., Sorella, S. & Becca, F. Superconductivity, charge-density waves, antiferromagnetism, and phase separation in the Hubbard-Holstein model. *Phys. Rev. B* **96**, 205145 (2017).

64. Ohgoe, T. & Imada, M. Competition among superconducting, antiferromagnetic, and charge orders with intervention by phase separation in the 2D Holstein-Hubbard model. *Phys. Rev. Lett.* **119**, 197001 (2017).

65. Hohenadler, M. & Batrouni, G. Dominant charge density wave correlations in the Holstein model on the half-filled square lattice. *Phys. Rev. B* **100**, 165114 (2019).

66. Georges, A., Kotliar, G., Krauth, W. & Rozenberg, M. J. Dynamical mean-field theory of strongly correlated fermion systems and the limit of infinite dimensions. *Rev. Mod. Phys.* **68**, 13 (1996).

67. Werner, P. & Millis, A. J. Efficient dynamical mean field simulation of the Holstein-Hubbard model. *Phys. Rev. Lett.* **99**, 146404 (2007).

68. Backes, S., Murakami, Y., Sakai, S. & Arita, R. Dynamical mean-field theory for the Hubbard-Holstein model on a quantum device. *Phys. Rev. B* **107**, 165155 (2023).

69. Shi, T., Demler, E. & Cirac, J. I. Variational approach for many-body systems at finite temperature. *Phys. Rev. Lett.* **125**, 180602 (2020).

70. Crawford, T. D. & Schaefer III, H. F. An introduction to coupled cluster theory for computational chemists. *Rev. Comput. Chem.* **14**, 33 (2007).

71. Mitchell, A. et al. *qiskit: An Open-Source Framework for Quantum Computing* (2021).

72. Wecker, D., Hastings, M. B. & Troyer, M. Progress towards practical quantum variational algorithms. *Phys. Rev. A* **92**, 042303 (2015).

73. Ortiz, G., Gubernatis, J. E., Knill, E. & Laflamme, R. Quantum algorithms for fermionic simulations. *Phys. Rev. A* **64**, 022319 (2001).

74. Wecker, D. et al. Solving strongly correlated electron models on a quantum computer. *Phys. Rev. A* **92**, 062318 (2015).

75. Verstraete, F., Cirac, J. I. & Latorre, J. I. Quantum circuits for strongly correlated quantum systems. *Phys. Rev. A* **79**, 032316 (2009).

76. Jiang, Z., Sung, K. J., Kechedzhi, K., Smelyanskiy, V. N. & Boixo, S. Quantum algorithms to simulate many-body physics of correlated fermions. *Phys. Rev. Appl.* **9**, 044036 (2018).

77. Costa, N. C., Seki, K., Yunoki, S. & Sorella, S. Phase diagram of the two-dimensional Hubbard-Holstein model: enhancement of *s*-wave pairing between charge and magnetic orders. *Commun. Phys.* **3**, 80 (2020).

78. de Leon, N. P. et al. Materials challenges and opportunities for quantum computing hardware. *Science* **372**, eabb2823 (2021).

79. Miessen, A., Ollitrault, P. J., Tacchino, F. & Tavernelli, I. Quantum algorithms for quantum dynamics. *Nat. Comput. Sci.* **3**, 25 (2023).

80. Shi, T., Cirac, J. I. & Demler, E. Ultrafast molecular dynamics in Terahertz-STM experiments: theoretical analysis using Anderson-Holstein model. *Phys. Rev. Res.* **2**, 033379 (2019).

81. White, S. R. & Feiguin, A. E. Real-time evolution using the density matrix renormalization group. *Phys. Rev. Lett.* **93**, 076401 (2004).

82. Linke, N. M. et al. Experimental comparison of two quantum computing architectures. *Proc. Natl Acad. Sci. USA* **114**, 3305 (2017).

Acknowledgements

Author contributions

Y.W. and E.D. conceived the project. M.M.D., A.M., H.Y., and Y.W. designed, implemented, and tested the code. M.M.D. led the data curation and analysis. M.M.D. and Y.W. wrote the paper with the help from I.T., T.N., and E.D.

Competing interests

The authors declare no competing interests.

Additional information

Supplementary information The online version contains supplementary material available at https://doi.org/10.1038/s42005-023-01353-3.

Correspondence and requests for materials should be addressed to Yao Wang.

Peer review information *Communications Physics* thanks the anonymous reviewers for their contribution to the peer review of this work. A peer review report is available.

Reprints and permission information is available at http://www.nature.com/reprints

Publisher's note Springer Nature remains neutral with regard to jurisdictional claims in published maps and institutional affiliations.